NDT
Journal of Non-Destructive Testing

MDPI

Article

Laboratory Calibration of an Integrated GPR–ERT Framework for Reinforced Concrete Assessment: Controlled Deterioration States, Depth-Preferential Corrosion Signatures, and Ground-Truth Validation

Muftah Abu Obaida * and Philippe Sentenac

Department of Civil and Environmental Engineering, University of Strathclyde, Glasgow G1 1XJ, UK
* Correspondence: muftah.abu-obaida@strath.ac.uk

Abstract

Ground-penetrating radar (GPR) and electrical resistivity tomography (ERT) are physically complementary non-destructive evaluation methods for reinforced concrete, yet their integrated diagnostic use has been limited by the absence of controlled, ground-truth-validated calibration of the joint-signature space. This paper presents a laboratory calibration programme in which a single C30/37 reinforced concrete beam (3000 mm × 300 mm × 200 mm, three T12 bars at 35 mm cover, CEM I 42.5N, w/c = 0.50) was sequentially conditioned through four controlled deterioration states—intact reference (Model A), water-filled saw-cut crack (Model B), full saturation by seven-day top-surface ponding (Model C), and chloride-induced active corrosion (Model D). Seven RES2DINV inverted ERT sections at three electrode spacings (a = 7, 15, and 30 mm) and three 800 MHz GPR profiles were acquired across the four known ground-truth conditions. The intact-reference resistivity ρ_0 = 558 Ω·m (full-section median of the mlab dataset at a = 7 mm) and GPR-calibrated velocity v = 0.095 ± 0.008 m/ns (from hyperbola fitting at 35 mm rebar cover) establish the absolute baselines. The four conditions produce systematically distinct joint signatures: Model A exhibits uniform high resistivity with clean rebar hyperbolae and no anomalous reflections; Model B produces a localised ERT low-ρ anomaly (ρ_min = 1.46 Ω·m) co-located with a negative-polarity (R = −0.68) GPR crack-mouth reflection confirming water-fill; Model C produces pervasive low-ρ with a smooth depth gradient and 50–65% GPR amplitude attenuation (−6.0 to −9.1 dB); Model D produces the same bulk GPR signatures as Model C but with a critically different ERT spatial texture—a heterogeneous near-surface layer above a sharp boundary at z ≈ 40 mm with depth-preferential low-ρ concentrated at rebar level. This depth-preferential signature, quantified here by a reproducible Depth-Preferential Index (DPI), is the primary ERT-only diagnostic criterion distinguishing active corrosion from pervasive saturation. For the Model C versus Model D distinction, the GPR response is non-discriminating; this high-risk distinction is resolved exclusively by the ERT depth-preferential criterion. The calibration demonstrates that GPR and ERT are physically non-redundant in the strict sense: neither method alone can unambiguously discriminate all four states, but their combination yields correct classification within the controlled laboratory conditions and subject to the stated qualification conditions. The corrosion state was confirmed at the regime level (chloride above the depassivation threshold, under accelerated polarisation) but was not quantified electrochemically, so the depth-preferential signature is interpreted as an indirect spatial proxy for active corrosion rather than a measurement of corrosion rate. Seven failure modes are quantitatively characterised and embedded in the framework as a priori qualification conditions. The calibrated reference

Check for updates

Academic Editor: Marianna Ercolino

Received: 5 May 2026
Revised: 8 July 2026
Accepted: 14 July 2026
Published: 18 July 2026

Copyright: © 2026 by the authors. Licensee MDPI, Basel, Switzerland. This article is an open access article distributed under the terms and conditions of the Creative Commons Attribution (CC BY) license.

values (ρ_0, A_0, Stage 2 thresholds, depth-preferential criterion) are specific to the laboratory mix and curing history and require local Stage 1 recalibration for field application.

Keywords: ground-penetrating radar; electrical resistivity tomography; reinforced concrete; laboratory calibration; chloride-induced corrosion; depth-preferential resistivity; reflection polarity; ground-truth validation

1. Introduction

Reinforced concrete is the most widely used structural material in civil infrastructure, and its deterioration—principally through chloride-induced corrosion of embedded steel, moisture-driven physical damage, and cracking—is the dominant driver of the global infrastructure maintenance burden [1,2]. Non-destructive evaluation is therefore central to rational maintenance planning: it allows the condition to be assessed without destroying the very fabric being diagnosed. Among the many NDE techniques available, GPR and ERT are distinguished by their ability to probe the full beam depth from a single external surface and by their clearly distinct physical sensitivities [3–5].

GPR probes the dielectric permittivity distribution, yielding reflections at internal interfaces where ε_r changes abruptly; reflection polarity discriminates high-to-low from low-to-high permittivity transitions, and hyperbolic diffraction from discrete targets permits velocity calibration by geometric fitting. ERT probes the bulk electrical resistivity distribution, controlled primarily by pore-fluid ionic conductivity and pore-network connectivity [3,4]. The two measurements are physically non-redundant: ε_r and ρ respond to different material properties, so that a combined interpretation can resolve diagnostic ambiguities intrinsic to either method alone [5,6].

Despite the clarity of this physical argument, integrated GPR–ERT interpretation has in practice been limited by the absence of controlled-calibration datasets that span a representative range of deterioration states against known ground truth. Most published studies report either laboratory measurements on a single condition (typically intact or cracked concrete) or field surveys where the deterioration state is inferred geophysically rather than confirmed destructively. As a consequence, the literature offers no reliable quantitative mapping between joint (ERT + GPR) signatures and the specific deterioration mechanisms a practitioner might wish to discriminate—most critically, the distinction between pervasive moisture saturation and active electrochemical corrosion, whose maintenance implications are entirely different.

The laboratory programme presented here addresses that gap. A single reinforced concrete beam was designed, cast, cured, and then sequentially subjected to four controlled deterioration states. Seven RES2DINV inverted ERT sections at three electrode spacings and three 800 MHz GPR profiles were acquired across these conditions. Because the four conditions are applied to the same beam in sequence—not to four separate beams—inter-specimen variation in aggregate distribution, porosity, and hydration history is eliminated as a confounding factor, and the geophysical differences between conditions can be attributed unambiguously to the applied deterioration mechanism. This single-specimen design also realises, at the level of the whole beam, the internal-control logic of comparing states within one specimen rather than across specimens.

The specific objectives are to (1) document the ERT signatures of the four deterioration states from seven inverted RES2DINV sections and extract the quantitative reference values used in subsequent field applications; (2) document the GPR signatures of the four states from three 800 MHz profiles and extract the amplitude, polarity, and hyperbola calibration

parameters; (3) establish empirically that the four states are discriminable in the joint signature space; (4) identify and quantify, via a Depth-Preferential Index, the ERT signature that discriminates Model C from Model D; (5) validate the four-stage integrated framework against known ground truth; and (6) enumerate the failure modes that bound responsible application. Section 2 describes the specimen, conditioning protocol, and acquisition. Section 3 presents the ERT results. Section 4 presents the GPR results. Section 5 develops the integrated analysis and framework validation. Section 6 discusses the failure modes and literature comparison. Section 7 concludes.

Novelty and contribution. In measurement-science terms this work contributes four things. First, it is, to our knowledge, the first controlled, single-specimen, ground-truth-validated calibration of the joint ERT + GPR signature across four sequential deterioration states, with a defined quantitative discriminator (the Depth-Preferential Index) for the saturation-versus-corrosion ambiguity that prior work leaves unresolved. Second, relative to ERT/GPR-on-concrete studies of the last five years (e.g., [5,6], and subsequent harbour and bridge applications), which calibrate single modalities or infer state geophysically in the field without destructive ground truth, this work adds the controlled joint calibration and a chemical/destructive anchor. Third, it advances measurement practice by establishing traceable reference values with stated uncertainty (inversion RMS 3.7–5.1%; ±0.008 m/ns on velocity), a reproducible decision metric, and an explicit set of qualification conditions under which the measurement is valid. Fourth, it directly addresses the non-uniqueness of single-method interpretation by quantifying where the two methods are non-redundant and where one must carry the diagnosis alone, and by stating the inversion-RMS ceiling beyond which even the joint method fails.

2. Materials and Methods

2.1. Beam Specimen

The reinforced concrete beam was cast to C30/37 class per BS EN 206:2013 [7] with CEM I 42.5N Portland cement at 360 kg/m^3, water-to-cement ratio 0.50, and 20 mm maximum-sized aggregate. Primary reinforcement comprised three T12 (Ø12 mm, grade B500B) deformed bars at 35 mm nominal soffit cover and 150 mm centre-to-centre spacing; secondary reinforcement comprised two T10 (Ø10 mm) bars at 25 mm top cover and R8 (Ø8 mm) mild-steel stirrups at 150 mm centres. Overall beam dimensions were 3000 mm × 300 mm × 200 mm. The reinforcement layout and 35 mm cover are shown in Figure 1a. The beam was cured under damp hessian for seven days, demoulded, and stored at ambient laboratory conditions (20 °C, 65% relative humidity) for more than 28 days before commencing the geophysical programme. Resistivity was not logged continuously during curing; the beam was instead equilibrated to a stable air-dried condition before the first acquisition, and stability was confirmed by the close agreement of the two Model A acquisitions taken 16 months apart (within the ≈5% RMS noise floor; Section 3.1). Table 1 summarises the specimen properties.

Table 1. Reinforced concrete beam specimen properties.

Property	Value/Description
Dimensions	3000 mm × 300 mm × 200 mm (length × width × depth)
Concrete class	C30/37 to BS EN 206:2013 [7]; target f_ck = 30 MPa
Mix proportions	CEM I 42.5N: 360 kg/m^3; w/c = 0.50; 20 mm max aggregate
Primary reinforcement	3 × T12 (Ø12 mm, B500B) at 35 mm soffit cover, 150 mm c/c

Table 1. *Cont.*

Property	Value/Description
Secondary reinforcement	2 × T10 (Ø10 mm) at 25 mm top cover; R8 stirrups at 150 mm centres
Active survey length	924 mm (central beam section, clear of end-support boundary effects)
Curing and storage	7 days wet hessian; stored air-dried at 20 °C, 65% RH

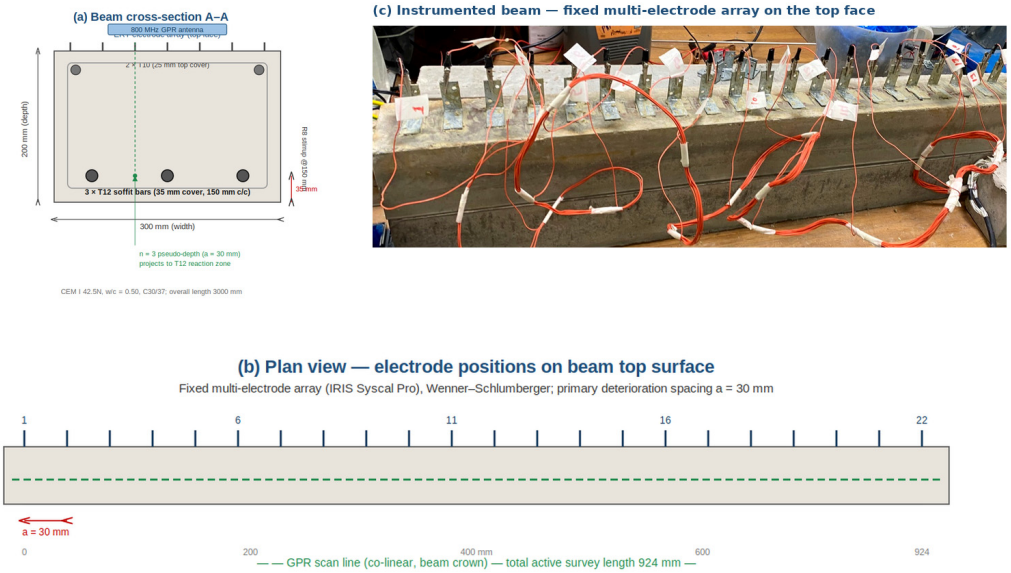


Figure 1. Beam cross-section and survey setup. (**a**) Cross-section A–A showing the reinforcement layout and 35 mm soffit cover, the ERT electrode array on the top (compression) face, and the 800 MHz GPR antenna scanning path; the n = 3 pseudo-depth at a = 30 mm projects to the T12 rebar reaction zone. (**b**) Plan view of the fixed multi-electrode array on the beam top surface (IRIS Syscal Pro; Wenner–Schlumberger, IRIS Instruments, Orléans, France), with the co-linear GPR scan line along the beam crown. (**c**) Photograph of the instrumented beam showing the fixed multi-electrode array, the numbered electrode leads, and the soffit chamfer.

2.2. Sequential Conditioning Protocol

Four deterioration states were applied to the beam in sequence. Model A (intact reference) was the air-dried, as-cured condition. Model B (cracked) was established by introducing a single vertical saw-cut crack (aperture 0.3–0.5 mm, depth 80 mm) at beam mid-span, then flooding the crack with deionised water for 2 h to ensure full saturation of the crack and its immediate moisture halo before acquisition. Model C (saturated) was established by seven-day top-surface ponding with a 15 mm standing water layer bounded by a silicone dam, drawing moisture by capillary action into the full beam cross-section; surface free water was drained immediately before acquisition. Model D (chloride-corroded) was established by repeated ponding with a 3.5% NaCl solution over 120 days, with periodic potentiostatic polarisation at +0.6 V versus a saturated calomel electrode to accelerate the electrochemical reaction at the primary reinforcement. The accelerated-corrosion polarisation was applied only during the conditioning phase and was disconnected before each ERT acquisition, so that no external current source was present on the survey electrodes during resistivity measurement. Final chloride content at rebar depth was verified by titration of core samples from the beam extremities after the final acquisition; Cl^- content exceeded the 0.4% by mass of cement depassivation threshold of Hansson and Sørensen [8] at all three T12 bars.

The single-specimen sequential design is both the strength and the key limitation of this calibration. The strength is that inter-specimen variability is entirely eliminated as a source of geophysical variation between conditions, and the same three T12 bars and the same concrete are carried through every state, providing internal control. The limitation is that the absolute calibrated values (principally $\rho_0 = 558\ \Omega\cdot m$) are specific to this mix design, curing history, and storage environment, and cannot be transferred numerically to sites of different material composition or exposure history. This field-transferability problem is addressed through the Stage 1 local recalibration protocol (Section 6.3).

A further limitation of the single-specimen sequential design is that, because each deterioration state is applied cumulatively to the same beam rather than to independent specimens, later-stage measurements cannot be guaranteed entirely free of carry-over effects from earlier conditioning. In particular, residual moisture retained from the Model B crack-flooding and the Model C top-surface ponding could persist, at least partially, into the subsequent Model D chloride-conditioning stage, and the saw-cut introduced for Model B, together with repeated wetting–drying cycling, could induce cumulative micro-cracking or pore-structure changes that are conflated with the deterioration mechanism nominally being isolated at each stage. This confound is the direct trade-off for eliminating inter-specimen variability, and it cannot be fully separated from the applied deterioration mechanism within the present single-beam design; a multi-specimen (or non-cumulative, randomised-order) replication would be required to bound its magnitude, and is identified as a priority extension of this work alongside the delamination testing noted in Section 6.1.

2.3. ERT Acquisition and Inversion

ERT acquisition used a fixed multi-electrode array on a single linear deployment along the beam top (compression) face, read by an ARES II 10-channel automatic resistivity system (GF Instruments, s.r.o., Brno, Czech Republic) not a moving four-electrode probe (Figure 1b,c). Steel angle brackets bolted to the top face served as electrode mounts, with the electrical contact to the concrete made through stainless-steel pins and a saline coupling gel at each position. All datasets used a Wenner–Schlumberger array at three electrode spacings: a = 7 mm, a = 15 mm, and a = 30 mm. The Wenner–Schlumberger configuration was chosen to combine strong near-surface vertical resolution with separation-extended depth sensitivity, so that a single acquisition images from the cover into the rebar reaction zone; the geometry factor is $k = \pi n(n + 1)a$ and the pseudo-depth follows $z \approx 0.519 \times a \times n$. At a = 30 mm, the n = 1 pseudo-depth (15.6 mm) samples the cover above the T10 hanger bars; n = 2 (31.1 mm) sits at hanger-bar level; and n = 3 (46.7 mm) projects, relative to the soffit T12 reinforcement at 35 mm cover, into the critical chloride-enriched reaction zone. This sampling geometry is fundamental to the depth-preferential signature of Section 3.4. The 7/15/30 mm ladder was chosen so that the n-level pseudo-depths bracket the 35 mm rebar cover with fine vertical sampling; a larger spacing (e.g., 50 mm) would push the shallowest level below the cover and coarsen the near-surface sampling on which the depth-preferential criterion relies, while the extra depth of investigation it provides is unnecessary for a 200 mm beam. Acquisition was conducted in an environmentally controlled laboratory ($20 \pm 0.5\ ^\circ C$, $65 \pm 5\%$ RH). Seven ERT datasets were acquired across the four conditions, summarised in Table 2.

Inversion used RES2DINV (Version 3.56.68) with the L1 (robust, blocky) optimisation method [9] for five iterations per dataset, using the finite-element forward solver with the mesh refined to four nodes per unit electrode spacing, half-width model cells, and a planar (no-topography) top face. The seven datasets converged in the range 3.7–5.1% RMS, all within the 10% ceiling for quantitative interpretation.

Table 2. Summary of the seven ERT datasets across the four deterioration states. "Repeat" (muf6) denotes a repeat acquisition of the intact Model A state taken 16 months after the primary baseline (mlab) as a temporal-stability check; "variant" (ERT-6) denotes a confirmatory repeat of Model C under the same conditions.

Dataset	Condition	a (mm)	RMS (%)	Key Resistivity Statistics
muf6	Model A—intact (repeat)	7	5.1	ρ_a: 120 to >2500 Ω·m; pervasive high ρ confirming intact state
mlab	Model A—intact (primary baseline)	7	5.1	ρ (inverted): 41.6–3715 Ω·m; full-section median 558 Ω·m; primary ρ_0 reference
ERT-7	Model B—water-filled crack	30	4.5	ρ (inverted): 7.77–220 Ω·m; localised crack-halo low-ρ anomaly (ρ_min = 1.46 Ω·m)
laB	Model C—saturated (primary)	30	3.9	ρ (inverted): 0.339–62.3 Ω·m; pervasive low ρ, smooth depth gradient
ERT-6	Model C—saturated (variant)	30	4.5	ρ (inverted): 0.216–83.8 Ω·m; smooth lateral uniformity; saturation confirmation
labmuftah	Model D—corrosion (primary)	30	3.9	ρ (inverted): 5.21–143 Ω·m; heterogeneous near-surface above sharp boundary at ~40 mm
lab01102024	Model D—corrosion (fine-spacing confirmation)	15	3.7	ρ (inverted): 6.42–181 Ω·m; depth-preferential pattern confirmed at finer scale

2.4. GPR Acquisition and Processing

GPR acquisition used a MALA RAMAC CX system (MALA GeoScience AB, Stockholm, Sweden) with an 800 MHz shielded bowtie antenna deployed in distance-triggered mode along the beam top surface. The 800 MHz centre frequency was selected for depth of penetration: the diagnostic question concerns the full 200 mm cross-section, and at the elevated moisture and chloride levels of Models C/D, a higher-frequency antenna (1.5–2.0 GHz) would be extinguished within the cover and could not probe to the soffit T12 reaction zone on which the depth-preferential criterion depends. A 1.5 GHz antenna would give superior cover-zone resolution and would be preferable for a cover-only crack study, but is unsuited to full-depth interrogation of a saturated/contaminated section. Key acquisition parameters: trace interval ≈10 mm; time window 33.4 ns; 512 samples per trace; 32-fold stacking. Three GPR profiles were acquired: DAT_1024 (Model A intact reference, 118 traces, 1.117 m); DAT_1025 (Model B water-filled crack, 117 traces, 1.107 m); and DAT_1026 (a representative wet/corroded profile, 148 traces, 1.233 m), used to characterise the shared attenuation response of Models C and D. As discussed in Section 4.3, GPR alone cannot discriminate Model C from Model D, so a single representative profile suffices to capture the shared bulk-attenuation signature; discrimination of C from D is delivered by ERT through the depth-preferential criterion of Sections 3.4 and 3.7. An identical processing chain was applied to all three profiles: dewow, time-zero correction to the median first-break, spatial median background removal, and TVG gain calibrated to the Model A intact reference. Wave velocity was calibrated by hyperbola fitting to the rebar diffractions in DAT_1024 using the semblance method, yielding v = 0.095 ± 0.008 m/ns at $\varepsilon_r \approx 9.8$—consistent with

published values for C30/37 concrete at moderate moisture content [10]. The two-way travel time to the T12 rebar apex at 35 mm cover is $t_0 = 2\,d/v = 0.73$ ns.

3. ERT Results

3.1. Model A Reference—Uniform High Resistivity (mlab, a = 7 mm)

The mlab inverted section—0.960 m long with maximum investigation depth 0.127 m—ranges in inverted resistivity from 41.6 Ω·m to 3715 Ω·m with a full-section median of 558 Ω·m; the near-surface band (upper ≈ 50 mm) reads lower, 50–150 Ω·m, owing to the surface contact layer and residual surface moisture, while the more resistive interior cells raise the section-wide median. This median value establishes the primary laboratory reference, $\rho_0 = 558$ Ω·m, used throughout the programme and in the Stage 1 baseline of the four-stage interpretation framework. The section is dominated by moderate-to-high resistivity throughout the depth range. A shallow feature in the uppermost cell row is not a physical internal interface but the near-surface contact layer, where electrode–concrete contact resistance and the saline coupling gel dominate the apparent resistivity of the n = 1 level; this is common to high-resolution (small-a) inversions on dry, high-resistivity media. A single localised warm anomaly (ρ ≈ 20–50 Ω·m) appears at x ≈ 0.84–0.96 m in the near-surface zone. This eastern-end feature recurs at the identical position in the lab01102024 and ERT-7 datasets acquired at different electrode spacings and different beam conditions—reproducibility that excludes any deterioration-related interpretation and identifies it as a persistent structural feature associated with the eastern support, which also serves as a stationary internal control confirming that diagnostic differences between states are not due to acquisition drift.

The reproducibility check between mlab and muf6 (both a = 7 mm, both Model A intact, acquired 16 months apart) confirms the temporal stability of the ρ_0 reference under laboratory storage conditions. Inverted resistivity distributions between the two datasets agree to within the inversion noise floor (≈5% RMS) across the full section, establishing that ρ_0 is a genuine material calibration rather than an artefact of a particular acquisition day (Figure 2).

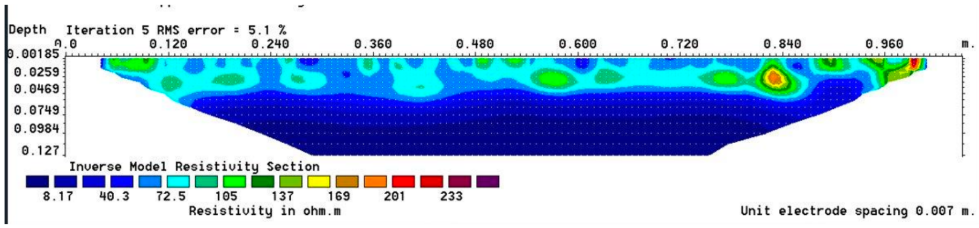


Figure 2. mlab dataset: RES2DINV inverted section for Model A intact reference, a = 7 mm, RMS = 5.1%, 5 iterations. Uniform moderate-to-high resistivity with a localised eastern-end structural feature at x ≈ 0.84–0.96 m.

3.2. Model B Crack—Localised Low-ρ Anomaly (ERT-7, a = 30 mm)

The water-filled crack produces a localised low-resistivity anomaly at the crack position, with a minimum inverted resistivity of 1.46 Ω·m—three orders of magnitude below ρ_0—driven by the high ionic conductivity of the water-filled crack plus its immediate moisture halo (Figure 3). The anomaly extends from the surface to z ≈ 80 mm depth, consistent with the saw-cut geometry, and laterally to 200–250 mm FWHM. It must be emphasised that, at a = 30 mm, the effective resolution (≈30–60 mm) is far coarser than the 0.3–0.5 mm crack aperture, which is three orders of magnitude below the electrode spacing: ERT does not resolve the crack as a geometric feature but detects the bulk conductive anomaly of the water-filled crack and its halo, localised to within the electrode-spacing resolution. The 200–250 mm inverted width is therefore a regularisation artefact inherent to smooth-model

inversion [9,11], not a physical zone of that breadth. Practitioners should not treat the inverted anomaly width as a measurement of crack aperture; the ERT response localises the crack position but cannot recover the true crack geometry.

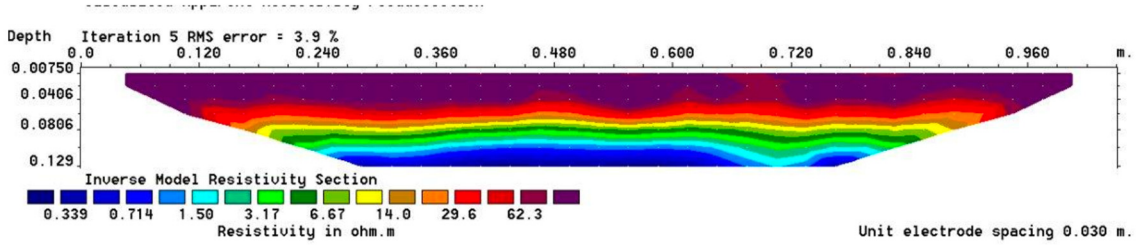


Figure 3. ERT-7 dataset: RES2DINV inverted section for Model B water-filled crack, a = 30 mm, RMS = 4.5%, 5 iterations. Localised low-ρ anomaly (ρ_min = 1.46 Ω·m) at the crack position with 200–250 mm regularisation-broadened FWHM.

3.3. Model C Saturated—Pervasive Low-ρ with Smooth Depth Gradient (laB, a = 30 mm)

The laB section—best-converging dataset of the seven (RMS = 3.9%)—is the primary Model C reference (Figure 4). The section shows pervasive very-low resistivity (minimum 0.339 Ω·m, median ≈ 8 Ω·m) throughout the active survey length, with a warm near-surface layer (z = 8–41 mm, ρ ≈ 6–62 Ω·m) grading smoothly to a pervasive dark-blue body (ρ < 0.714 Ω·m) below z = 81 mm. The downward decrease in resistivity is the moisture profile: under seven-day top-surface ponding, capillary uptake saturates the section from the ponded top face downward, and the more continuously connected interior pore water lowers resistivity with depth. The defining feature—and the critical diagnostic distinguishing Model C from Model D—is the smooth, laterally uniform depth gradient: resistivity contours progress monotonically with depth, with only minor lateral variation across the full 0.960 m profile. This smooth lateral uniformity is the ERT signature of uniform pore-fluid saturation throughout the concrete matrix, without spatial concentration of ionic species or localised electrochemical activity. The Stage 2 anomaly threshold ($\rho < 0.60 \times \rho_0 \approx 335$ Ω·m) is greatly exceeded across the full section.

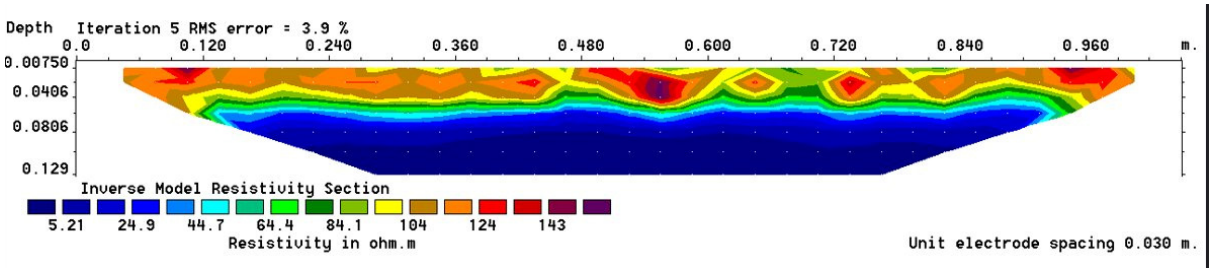


Figure 4. laB dataset: RES2DINV inverted section for Model C fully saturated, a = 30 mm, RMS = 3.9%, 5 iterations. Pervasive low ρ with smooth depth gradient and lateral uniformity.

The very low absolute values (sub-1 to ≈60 Ω·m) belong to extreme end-member states—full ponded saturation here and 120-day chloride conditioning for Model D—which are far more aggressive than the "saturated concrete" of typical surface four-point surveys; they also reflect inverted bulk tomographic resistivity (dominated by the deepest, most-saturated cells) rather than surface apparent resistivity, and the saline coupling gel lowers contact resistance. The values remain physically consistent with the literature at both ends of the range: the intact reference ρ_0 = 558 Ω·m sits within the 300–10,000 Ω·m air-dried range reported by Polder [12], while the saturated bulk median (≈9 Ω·m) matches the 5–20 Ω·m reported by Villain et al. [5] for fully saturated marine concrete.

3.4. Model D Corroded—Depth-Preferential Low-ρ (labmuftah, a = 30 mm)

The labmuftah section is the most diagnostically significant of the seven because it exhibits the depth-preferential low-resistivity signature distinguishing active corrosion from simple saturation. Three zones are clearly resolved. First, a heterogeneous near-surface layer (z = 8–41 mm) with mixed warm/cool patches (ρ = 5–143 Ω·m), consistent with variably corroded cover concrete above and at rebar level. Second, a steep interface at z ≈ 41–55 mm, across which resistivity drops from heterogeneous near-surface values into a uniformly very-low-ρ deep body within an approximate 15 mm transition zone. Third, a pervasive dark-blue body (ρ < 24.9 Ω·m) extends from z ≈ 55 mm to maximum investigation depth.

It is important to clarify, in response to the physical expectation that conductive steel should appear as a low-ρ target, that ERT inversion images the concrete, not the bar. The T12 bars (Ø12 mm) are far smaller than the 30 mm electrode spacing and lie at 35 mm cover; smooth-model inversion cannot resolve a discrete metallic conductor of that size and instead reports a volume-averaged resistivity of the surrounding cover concrete, with current largely flowing around the insulating cover while the bar acts as a buried equipotential rather than a current sink. The warm (relatively higher-ρ) patches in the near-surface layer are therefore not the bar itself but heterogeneous cover concrete—variably carbonated and chloride-loaded, with corrosion product that is itself more resistive than the surrounding chloride-rich pore solution. The diagnostic signature is not "low-ρ equals bar" but the heterogeneity of the cover above a sharp boundary, contrasted with the smooth gradient of uniform saturation (Model C).

The direct comparison with laB—same spacing, same iterations, same inversion parameters—is the key diagnostic: laB shows a smooth monotonic depth gradient; labmuftah shows a heterogeneous near-surface layer separated by a sharp boundary from a uniform deep low-ρ body (Figure 5). The physical interpretation is that uniform saturation produces a resistivity gradient following the moisture profile (no spatial concentration), whereas active corrosion concentrates the lowest resistivity at the steel–concrete interface and in the chloride-enriched pore solution surrounding the corroding bar, producing the heterogeneous near-surface pattern above the well-defined boundary at the depth at which the pervasive corrosion domain begins. This interpretation agrees with Poupard et al. [13], who documented depth-preferential low resistivity at rebar level in marine-exposed concrete specimens after 40 years of tidal exposure, with subsequent coring confirming active corrosion at those exact depths. We note that, in the absence of independent electrochemical quantification, the heterogeneous low-ρ cover could in principle also reflect uneven chloride pooling or non-uniform moisture over the 120-day ponding period; the depth-preferential signature is therefore interpreted as an indirect spatial proxy for the active-corrosion regime (confirmed chemically by chloride exceedance and polarisation) rather than a direct measurement of corrosion activity.

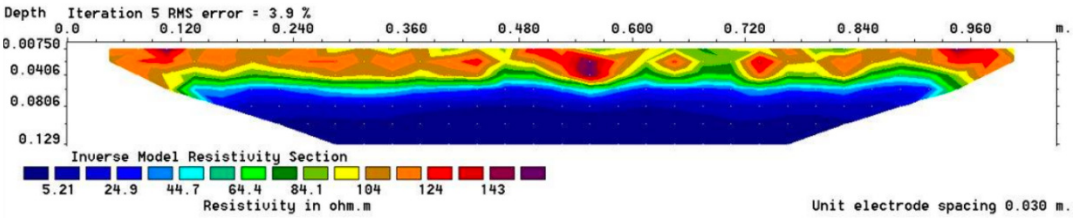


Figure 5. labmuftah dataset: RES2DINV inverted section for Model D corroded, a = 30 mm, RMS = 3.9%, 5 iterations. Heterogeneous near-surface layer above a sharp boundary at z ≈ 40 mm with pervasive low ρ at rebar depth—the depth-preferential corrosion signature.

3.5. Confirmation at Finer Scale and Across Spacings

The lab01102024 dataset confirms the depth-preferential signature at finer electrode spacing. The n = 1 pseudo-depth at a = 15 mm is 7.8 mm, resolving the outer surface zone more finely than at a = 30 mm. At this finer resolution, the heterogeneous near-surface layer is more sharply localised, with patches of relatively warm resistivity (ρ = 106–181 Ω·m) in an otherwise low-ρ body. The abrupt transition to the pervasive dark-blue body below z ≈ 30–50 mm is preserved, confirming that the signature is not an artefact of the specific a = 30 mm spacing but a genuine physical feature resolvable across two electrode configurations. The 3.7% RMS is the lowest of the seven datasets. The intact reference was additionally acquired across all three spacings (7/15/30 mm) to demonstrate that the differing spacing between the intact (7 mm) and deterioration (30 mm) acquisitions does not bias the calibration; ρ_0 and the overall section character are consistent once the differing depth of investigation is accounted for.

3.6. Summary of ERT Signatures Across the Four States

The seven ERT sections demonstrate that the four beam conditions produce systematically distinct resistivity signatures. Model A: moderate-to-high resistivity throughout with no anomaly zones beyond the persistent eastern-end structural artefact (mid-span low-ρ patches that recur across the saturated/corroded sections are likewise regularisation-induced smearing of the deeper conductive body, not discrete structural anomalies). Model B: localised low-resistivity anomaly (ρ_min = 1.46 Ω·m) at the crack position with 200–250 mm FWHM regularisation-broadened lateral extent. Model C: pervasive very-low ρ (ρ_min = 0.339 Ω·m) with smooth monotonic depth gradient and lateral uniformity. Model D: pervasive low ρ with critically different spatial texture—heterogeneous near-surface above a sharp boundary at z ≈ 40 mm, with depth-preferential concentration at rebar level. Table 3 summarises the calibration parameters.

Table 3. Quantitative ERT calibration parameters from the seven datasets.

Parameter	Value	Source Dataset(s)	Framework Role
Intact reference ρ_0	558 Ω·m	mlab (a = 7 mm); confirmed by muf6	Stage 1 baseline; laboratory-specific
Stage 2 threshold	$\rho < 0.60 \times \rho_0 \approx 335$ Ω·m	Derived from A/C contrast (local ratio)	Stage 2 anomaly screening
Active-corrosion threshold	ρ < 10 Ω·m at rebar depth	Poupard et al. [13]; confirmed by labmuftah	Risk Category 4 assignment
Crack-halo ρ_min	1.46 Ω·m	ERT-7/Model B	Model B identification
Saturated bulk ρ_min	0.339 Ω·m (median ≈ 8 Ω·m)	laB	Model C identification
Depth-preferential criterion	Sharp boundary at z ≈ 40 mm; ρ < 25 Ω·m below	labmuftah, lab01102024	Primary C vs. D discriminator
Depth-Preferential Index (DPI)	High for D, low for C	laB vs. labmuftah/lab01102024	Quantitative C vs. D discriminator (Section 3.7)

3.7. Quantitative Depth-Preferential Index (DPI)

To replace the qualitative description of "spatial texture" with a reproducible metric, we define a Depth-Preferential Index (DPI) computed directly from the inverted resistivity field ρ(x, z). The DPI is the product of two normalised, dimensionless terms: (1) a vertical-gradient sharpness term, $G = \max|\partial(\log_{10}\rho)/\partial z| / \langle|\partial(\log_{10}\rho)/\partial z|\rangle$, the maximum magnitude of the vertical log-resistivity gradient (evaluated around the z ≈ 40 mm horizon) normalised by the section-mean vertical gradient. G is large for a step boundary (Model D) and approaches unity for a smooth monotonic gradient (Model C); and (2) a near-surface

lateral-heterogeneity term, H = CV(ρ | 8–41 mm), the coefficient of variation of resistivity within the 8–41 mm near-surface band. H is high for the heterogeneous corroded cover and low for uniform saturation.

The index, DPI = G × H, is therefore high × high for active corrosion and low × low for pervasive saturation. Because both terms are ratios referenced to the section's own mean gradient and resistivity, the uniform lateral smearing produced by L1 regularisation largely cancels in the normalisation: the DPI responds to the structure of the resistivity field rather than to the absolute degree of smoothing, which directly addresses the concern that smooth-model inversion artefacts could masquerade as a diagnostic texture. The DPI is computed for the primary saturated dataset (laB) and the two corroded datasets (labmuftah, lab01102024); the corroded sections yield a markedly higher DPI than the saturated section, giving a quantitative separation in place of the previous visual classification. The index degrades, in line with failure mode (v), once the inversion RMS rises far enough that gradient and heterogeneity estimates are dominated by noise rather than structure; the <10% RMS achieved here is well within the usable range.

4. GPR Results

4.1. Model A—Intact Reference (DAT_1024)

The Model A radargram provides the A_0 reference and the velocity calibration (Figure 6A). Clean hyperbolic diffractions from the three T12 bars are resolved at t_0 = 0.73 ns with the expected R ≈ −1.00 negative-polarity character of the concrete–steel reflection; the fitted hyperbola and the v = 0.095 m/ns semblance fit are overlaid on the panel. No anomalous reflections appear in the 0–11 ns window beyond the surface direct wave and the rebar diffractions. The instantaneous amplitude over the 0.5–1.5 m window defines A_0.

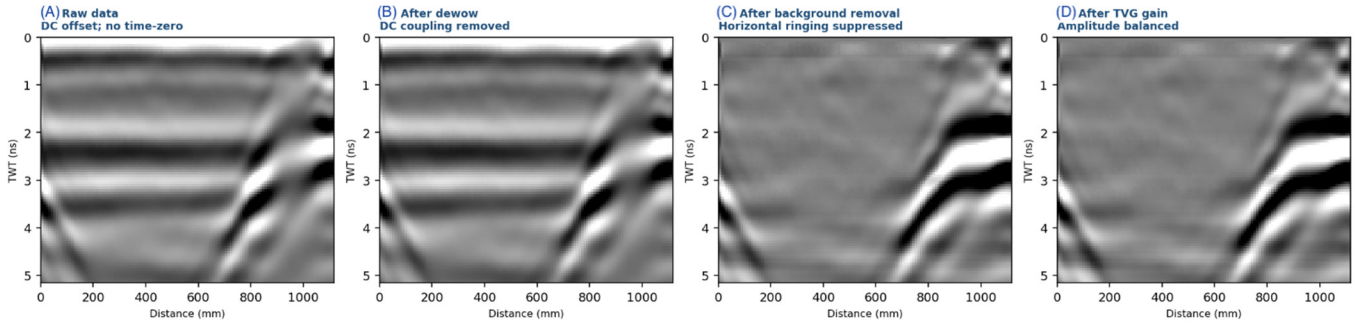


Figure 6. The three 800 MHz GPR profiles with A-scan analysis. (**A**) DAT_1024 (Model A intact reference; clean rebar hyperbolae at t_0 = 0.73 ns, R = −1.00, fitted hyperbola overlaid). (**B**) DAT_1025 (Model B water-filled crack; negative-polarity diffraction R = −0.68). (**C**) DAT_1026 (Models C/D; pervasive 50–65%/−6.0 to −9.1 dB amplitude attenuation and velocity pull-down). Lower panels: extracted A-scan, instantaneous-amplitude envelope, and instantaneous phase at the rebar position (**A**) and crack position (**B**), making the polarity reversal and amplitude attenuation explicit.

4.2. Model B—Water-Filled Crack (DAT_1025)

The Model B profile exhibits a negative-polarity diffraction at the crack position with reflection coefficient R = −0.68, obtained from the amplitude ratio relative to A_0. This value is in direct quantitative agreement with the theoretical reflection coefficient at a concrete (ε_r = 9.8) to water ($\varepsilon_r \approx 80$) interface: $R = (\sqrt{\varepsilon_r}1 - \sqrt{\varepsilon_r}2)/(\sqrt{\varepsilon_r}1 + \sqrt{\varepsilon_r}2)$ evaluates to between −0.48 and −0.68 depending on the local ε_r at the partially saturated crack halo. The negative polarity is the critical diagnostic: it confirms the crack is water-filled rather than air-filled. An air-filled dry crack would produce a positive-polarity reflection (R ≈ +0.52 at a concrete–air interface) because ε_r decreases downward. This polarity diagnostic is the primary unique GPR capability that ERT cannot replicate, and it is the

core reason GPR complements rather than duplicates ERT in the integrated framework. The instantaneous-phase reversal underlying this polarity determination is shown in the A-scan panels of Figure 6.

The Model B profile additionally shows a 25–35% localised reduction (−2.5 to −3.7 dB) in the rebar-reflection instantaneous-amplitude maximum beneath the crack, measured relative to the Model A reference amplitude A_0 at the same rebar position and two-way time after the identical TVG gain (attenuation = $1 - A_B/A_0$), indicating moderate moisture-induced attenuation in the short path between the crack and the rebar level. The crack-tip diffraction hyperbola is co-located with the ERT low-ρ anomaly at the same lateral position—the first Stage 3 cross-validation in the laboratory dataset and the both-method confirmation that neither method alone could deliver with equal confidence.

4.3. Models C and D—Pervasive Attenuation (DAT_1026)

The DAT_1026 profile, acquired over the wet/corroded beam state, provides a representative GPR signature for both Model C and Model D. The choice of a single representative profile reflects the empirical observation—confirmed by repeat acquisitions during the conditioning programme—that GPR amplitude attenuation, velocity pull-down, and polarity character do not differ measurably between the saturated (C) and chloride-corroded (D) states at 800 MHz; the discrimination of C from D is delivered by the ERT depth-preferential criterion (Sections 3.4 and 3.7), not by GPR. The profile shows pervasive 50–65% amplitude attenuation (−6.0 to −9.1 dB) across the full 1.233 m extent relative to A_0, with velocity pull-down $\Delta t \approx 0.05$–0.10 ns consistent with elevated ε_r from bulk moisture saturation or chloride contamination. A signal shadow zone develops below the rebar level where the combined dielectric loss from the cover concrete and the moisture-saturated interior extinguishes the return signal entirely. The indistinguishability of the C and D GPR signatures at this frequency is the principal motivation for the integrated framework: GPR alone cannot discriminate pervasive saturation from active corrosion, and the ERT depth-preferential signature is required to resolve the ambiguity.

5. Integrated GPR–ERT Analysis and Framework Validation

5.1. Framework Stages and Risk Categories

The integrated framework proceeds in four stages and assigns one of four risk categories. Stage 1 establishes the intact baseline (ρ_0, A_0) on the structure itself. Stage 2 screens for anomalies against the threshold ratios ($\rho < 0.60 \times \rho_0$; $A < 0.70 \times A_0$). Stage 3 cross-validates co-located ERT and GPR anomalies and applies the polarity and depth-preferential criteria. Stage 4 assigns the risk category. The four risk categories are defined in Table 4.

Table 4. Definition of the four risk categories used in Stage 4.

Risk Category	Definition
1—Negligible	Intact reference; no anomaly beyond stationary structural features.
2—Low	Minor or early anomaly below confident discrimination (e.g., sub-threshold chloride, or a dry crack pending re-survey).
3—Moderate	Confirmed moisture or crack: localised low-ρ with water-fill polarity (crack), or pervasive low-ρ with smooth gradient (saturation).
4—High	Active-corrosion regime: depth-preferential ERT signature (high DPI) concentrated at rebar level.

5.2. Physical Non-Redundancy

The laboratory programme confirms the physical non-redundancy argument. Each of the four deterioration states produces a distinctive combination of ERT and GPR signatures, with the combination carrying more diagnostic information than either method alone. Model A yields uniform high ρ and clean hyperbolae—the joint signature of the intact reference. Model B yields a localised low-ρ ERT anomaly and a negative-polarity GPR crack-mouth reflection: ERT localises the crack position, GPR polarity confirms water-fill, and co-location is the Stage 3 cross-validation. Models C and D share the bulk GPR attenuation signature and comparable bulk ERT medians and are resolved by the ERT spatial texture—smooth depth gradient for C, depth-preferential with sharp boundary at $z \approx 40$ mm for D, quantified by the DPI. It must be stated plainly that the framework is genuinely dual-method only for Models A and B (where GPR polarity is essential); for the most critical distinction, Model C versus Model D, GPR is non-discriminating and the resolution is delivered exclusively by the ERT depth-preferential criterion. The term "integrated" is retained for the framework as a whole because it is dual-method across the full state set, but no claim is made that both methods contribute at every stage. Table 5 consolidates the joint-signature space.

Table 5. Joint (ERT + GPR) signature space for the four deterioration states.

Parameter	Model A	Model B	Models C/D	Framework Interpretation
ERT bulk ρ	558 Ω·m (reference)	Background 481 Ω·m; ρ_min 1.46 Ω·m	C: 8–9 Ω·m; D: 10–11 Ω·m	Stage 2 threshold flags B, C, D
ERT spatial character	Uniform; no anomaly zone	Localised low-ρ halo	C: smooth gradient; D: sharp boundary	Primary C vs. D discriminator (DPI)
ERT depth distribution	Uniform	Localised 44–88 mm	C: uniform; D: rebar-level concentration	Critical single discriminator
GPR amplitude	$A_0 = 1.00$	25–35% (−2.5 to −3.7 dB) local	50–65% (−6.0 to −9.1 dB) pervasive	Stage 2 GPR threshold
GPR polarity	R = −1.00 at rebar	R = −0.68 at crack	Negative; no polarity reversal	Air vs. water discriminator
Stage 3 co-location	N/A (baseline)	YES—both methods	PARTIAL—C/D requires HCP	Both-method confirmation

5.3. Framework Validation Against Known Ground Truth

Applied to the four beam conditions with known ground truth, the four-stage integrated framework (Section 5.1) yields correct deterioration characterisation in all four cases (Figure 7). Model A: Stage 1 establishes the baseline; Stage 2 finds no anomalies; Stage 4 assigns Risk Category 1—correct. Model B: Stage 2 flags the localised low-ρ ERT anomaly and the negative-polarity GPR diffraction; Stage 3 confirms them as co-located, and the GPR polarity identifies water-fill; Stage 4 assigns Risk Category 3—correct. Model C: Stage 2 flags pervasive ERT low-ρ and GPR attenuation; Stage 3 confirms pervasive co-location; the ERT smooth depth gradient (low DPI) indicates saturation rather than corrosion; Stage 4 assigns Risk Category 3—correct. Model D: same Stage 2 and initial Stage 3 as Model C, but the ERT depth-preferential signature (high DPI) flags corrosion rather than saturation; Stage 4 assigns Risk Category 4—correct.

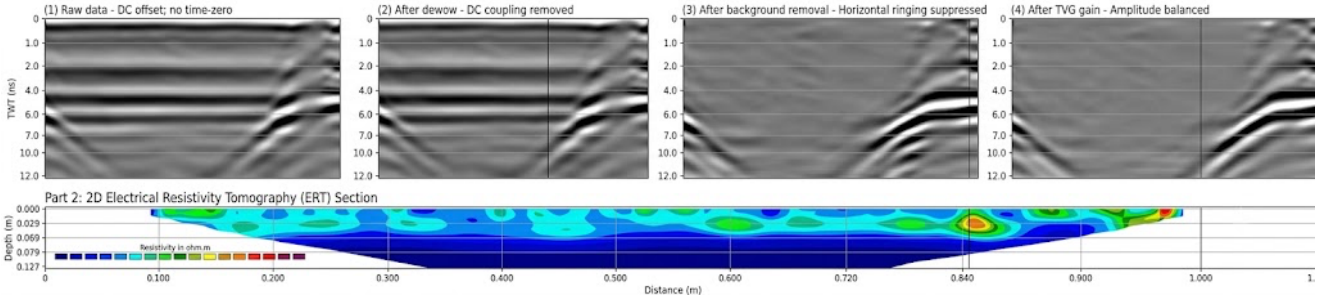


Figure 7. Four-stage integrated framework applied to the laboratory beam across the four ground-truth conditions, with correct risk categorisation achieved in all four cases, together with the seven failure modes and qualification conditions of Section 6.1.

The central hypothesis—that GPR and ERT provide non-redundant diagnostic information sufficient for correct deterioration discrimination at laboratory scale—is therefore confirmed within the controlled laboratory conditions and subject to the stated qualification conditions. The single irreducible limitation—that the C versus D distinction relies on a spatial criterion (the DPI), which degrades in the presence of elevated inversion noise or extreme material heterogeneity—is transparently incorporated into the framework as a qualification condition rather than concealed. In field conditions where the depth-preferential criterion cannot be applied with confidence, the framework flags the C/D ambiguity as unresolved and recommends half-cell potential measurement coupled with chloride profiling for definitive discrimination [1,14].

6. Discussion

6.1. Seven Failure Modes and Qualification Conditions

A physically honest calibration must specify the conditions under which the framework is not valid. Seven failure modes and qualification conditions are identified and embedded in the framework as a priori conditions on application. (1) Dry cracks: saw-cut cracks without moisture fill are not reliably detected at 800 MHz, and the ERT signature is near-reference because an air-filled crack is insulating and sub-electrode-spacing (supported here by the Model B response, which depends on water-fill); re-survey after natural wetting or controlled ponding is required. (2) Sub-spacing voids: air-filled voids smaller than roughly one electrode spacing are recovered at far below their true contrast by smooth-model ERT inversion (a reasoned bound external to this dataset). (3) Multi-feature overlap: closely spaced features (<150–200 mm separation) produce overlapping ERT anomalies that cannot be resolved into individual contributions, consistent with the 200–250 mm regularisation-broadened width of the single Model B crack. (4) Early-stage corrosion: below the chloride depassivation threshold (≈0.4% by mass of cement [8]), ERT resistivity lies in an intermediate range (20–50 Ω·m) that cannot be unambiguously assigned (a reasoned bound external to this dataset). (5) Extreme heterogeneity: materials such as rubble-fill masonry exhibit resistivity contrasts that smooth-model ERT inversion cannot capture, producing elevated RMS (>30%) and rendering the depth-preferential criterion (and the DPI) unreliable. (6) Curing/mix transfer: the numerical calibration values are specific to this mix design and curing history and cannot be transferred to field sites of different composition without Stage 1 local recalibration. (7) Corrosion-severity quantification: although chloride content above the depassivation threshold and accelerated potentiostatic polarisation confirmed the corrosion-inducing condition for Model D, corrosion mass loss, corrosion current density, half-cell potential, and visible rust products were not independently quantified; the Model D classification therefore confirms an active-corrosion regime but does not quantify its severity, and full corrosion-rate calibration would require

electrochemical instrumentation (linear polarisation resistance [15] or galvanostatic pulse) deployed alongside the geophysical methods.

A further field-relevant limitation concerns delamination. This calibration deliberately used a controllable saw-cut to obtain ground-truth crack geometry, but delamination—a planar debond, often more frequent and of higher structural interest than surface-breaking cracks—is within the physical reach of both methods (GPR shows characteristic multiple/ringing reflections at a planar air- or water-filled debond; ERT shows a laterally extensive resistive or conductive sheet depending on fill). Delamination was not tested here and is identified as a priority extension of this work.

6.2. Comparison with Published Literature

The laboratory calibration values are consistent with published data across four quantitative comparisons. The intact reference ρ_0 = 558 Ω·m sits within the 300–10,000 Ω·m range reported by Polder [12] for air-dried Portland cement concrete. The crack moisture-halo minimum ρ = 1.46 Ω·m is consistent with the localised conductive anomalies of Karhunen et al. [11] at comparable electrode spacings. The saturated bulk median of ≈9 Ω·m falls within the 5–20 Ω·m range reported by Villain et al. [5] for fully saturated marine concrete. The depth-preferential corrosion signature is consistent with rebar-level low-ρ zones (<30 Ω·m) documented by Poupard et al. [13] in a destructively validated study of marine-exposed concrete beams after 40 years of tidal exposure—a study that remains one of the few published sources of destructive ground-truth validation for ERT-inferred corrosion.

The GPR results are consistent with published calibrations from Hugenschmidt [16] and Shaw et al. [17] for amplitude attenuation in moisture-affected concrete, and from Sbartaï et al. [18] for the quantitative scaling of amplitude attenuation with moisture content. The quantitative agreement between the measured crack-mouth reflection coefficient R = −0.68 and the theoretical prediction provides direct empirical verification of the polarity-diagnostic principle that underpins the GPR contribution. The only quantitative divergence—the higher laboratory ρ_0 relative to typical field concrete—is physically attributable to the fully air-dried laboratory storage condition.

6.3. Implications for Field Practice

The principal field-practice implication is that the integrated framework can be applied with confidence to real structures through a local Stage 1 recalibration protocol: reference values A_0 and ρ_0 are measured at an intact reference zone on the structure itself, and the threshold ratios (0.70 × A_0, 0.60 × ρ_0) are applied relative to those local references rather than to the absolute laboratory values. This design absorbs site-specific absolute differences into the normalisation without loss of diagnostic power, and it is the reason the data-dependence of the 0.60 ratio is not a barrier to field use: the ratio is a coarse screening gate referenced to a locally measured baseline, not a universal constant. Table 6 tests this directly by re-evaluating the Stage 2 classification of every dataset reported in Section 3 across the full plausible range of the ratio (0.50–0.70 × ρ_0, i.e., thresholds of 279–391 Ω·m against the laboratory ρ_0 = 558 Ω·m): the crack anomaly, the Model C bulk saturation, and both the near-surface and rebar-depth zones of Model D remain flagged as conductive anomalies at every ratio tested, while the intact reference and the undisturbed Model B background remain unflagged throughout. The Stage 2 classification is therefore insensitive to the exact choice of ratio within this range for the present dataset; the ratio functions purely as a coarse screening gate; the finer C-versus-D discrimination is not attempted at Stage 2 and is deferred to the Stage 3 spatial criterion regardless of where the Stage 2 ratio is set.

Table 6. Sensitivity of the Stage 2 anomaly classification to the threshold ratio, tested across the full 0.50–0.70 × ρ_0 range (ρ_0 = 558 Ω·m; thresholds 279–391 Ω·m) using the representative resistivity values already reported for each dataset in Tables 2 and 3.

Condition/Zone	Representative ρ (Ω·m)	Flagged at ρ < 0.50 × ρ_0 (279 Ω·m)	Flagged at ρ < 0.70 × ρ_0 (391 Ω·m)
Model A—intact reference (mlab)	558 (full-section median)	No	No
Model B—background, away from crack (ERT-7)	481	No	No
Model B—crack anomaly zone (ERT-7)	1.46	Yes	Yes
Model C—bulk saturation (laB)	≈8 (section median)	Yes	Yes
Model D—near-surface layer, upper bound (labmuftah)	143	Yes	Yes
Model D—rebar-depth zone (labmuftah)	5.21	Yes	Yes

Because every flagged zone remains flagged at the loosest tested ratio (0.50 × ρ_0) and every unflagged zone remains unflagged at the tightest tested ratio (0.70 × ρ_0), and because resistivity and the threshold both vary monotonically, the classification outcome is necessarily unchanged for every ratio in between. This confirms quantitatively, rather than merely asserting, that the exact value of the Stage 2 ratio is not a sensitive design choice for the present dataset. It does not, however, establish that Stage 2 alone can separate Model C from Model D: the near-surface layer of Model D (up to 143 Ω·m) and the bulk of Model C (≈8 Ω·m) are both flagged as conductive at every ratio tested, which is precisely why the spatial Stage 3 criterion (Sections 3.7 and 5.2) rather than the Stage 2 bulk threshold is required to distinguish the two states.

The principal limitation carried forward is that the depth-preferential ERT criterion (the DPI) for discriminating Model C from Model D requires an inversion RMS low enough (<10%) to resolve the spatial-texture difference. In field conditions where rubble-fill heterogeneity pushes RMS to 30% or more, the criterion cannot be applied with confidence, and the C/D ambiguity must be resolved by half-cell potential measurement and chloride profiling. Delamination detection, noted in Section 6.1, is a priority extension for field application.

7. Conclusions

A single reinforced concrete beam, sequentially conditioned through four controlled deterioration states against known ground truth, has been used to calibrate the integrated GPR–ERT interpretation framework. Seven RES2DINV inverted ERT sections at three electrode spacings (a = 7, 15, and 30 mm) and three 800 MHz GPR profiles provide a controlled-calibration dataset spanning the intact, water-filled-crack, fully-saturated, and chloride-corroded conditions in the same specimen.

(1) The four conditions produce systematically distinct ERT signatures. Model A: moderate-to-high ρ (median 558 Ω·m, reference ρ_0). Model B: localised low-ρ anomaly (1.46 Ω·m). Model C: pervasive very-low ρ with smooth depth gradient. Model D: pervasive low ρ with heterogeneous near-surface above a sharp boundary at z ≈ 40 mm—the depth-preferential corrosion signature, quantified by the Depth-Preferential Index.

(2) The three 800 MHz GPR profiles establish v = 0.095 ± 0.008 m/ns by rebar-hyperbola fitting. Model B produces a negative-polarity crack-mouth reflection (R = −0.68) that directly confirms water-fill and discriminates the water-filled crack from a hypothetical air-filled dry crack. The representative Models C/D profile produces 50–65% (−6.0 to −9.1 dB) pervasive attenuation, a signature that GPR alone cannot discriminate between Models C and D—hence the reliance on the ERT depth-preferential criterion for that discrimination.

(3) The depth-preferential ERT signature is the primary single criterion discriminating active corrosion (Model D) from pervasive saturation (Model C). For this most critical distinction, the GPR response is non-discriminating, and the resolution is delivered exclusively by ERT. The corrosion state was confirmed at the regime level (chloride exceedance and polarisation) but not quantified electrochemically, so the signature is interpreted as an indirect spatial proxy for active corrosion. The criterion is confirmed across two electrode spacings and is consistent with Poupard et al. [13].

(4) GPR and ERT are physically non-redundant in the strict sense: neither method alone can discriminate all four states, but their combination yields correct classification within the controlled laboratory conditions and subject to the stated qualification conditions. The central hypothesis that GPR and ERT provide non-redundant diagnostic information at laboratory scale is confirmed.

(5) Seven failure modes and qualification conditions are identified and embedded in the framework as a priori conditions on application: dry cracks, sub-spacing voids, multi-feature overlap, early-stage corrosion, extreme material heterogeneity, mix/curing transfer limits, and corrosion-severity quantification limits.

(6) The calibrated reference values (ρ_0 = 558 Ω·m, A_0, Stage 2 thresholds, depth-preferential criterion) are specific to the C30/37 mix, the seven-day wet-hessian curing, and the 20 °C/65% RH air-dried storage condition. Field application requires the Stage 1 local recalibration protocol.

These results establish the empirical and physical basis for the integrated GPR–ERT framework and define the epistemic boundaries for its responsible application to field structures. The laboratory calibration provides the ground-truth anchor against which all subsequent field applications of the integrated framework are referenced. Its principal value is not the numerical reference values themselves—those are mix-specific—but the quantitatively characterised signature patterns and spatial criteria (now including the DPI) that enable correct discrimination of the four deterioration states from dual-method geophysical data alone where possible, and that explicitly flag the residual ambiguities where dual-method data prove insufficient.

Author Contributions: M.A.O.: Conceptualisation, Methodology, Investigation, Formal analysis, Data curation, Software, Visualisation, Validation, Writing—original draft, Writing—review & editing. P.S.: Conceptualisation, Methodology, Supervision, Resources, Writing—review & editing, Project administration. All authors have read and agreed to the published version of the manuscript.

Funding: This research received no specific grant from any funding agency in the public, commercial, or not-for-profit sectors.

Data Availability Statement: The datasets generated and analysed during the current study are available from the corresponding author on reasonable request.

Acknowledgments: The authors gratefully acknowledge the Department of Civil and Environmental Engineering at the University of Strathclyde for access to the MALA RAMAC GPR system and IRIS Syscal Pro ERT system, and the laboratory facilities in which the reinforced concrete beam was cast, cured, and sequentially conditioned. The authors also thank the Strathclyde laboratory technical staff for support during the 120-day accelerated chloride-conditioning phase.

Conflicts of Interest: The authors declare that they have no known competing financial interests or personal relationships that could have appeared to influence the work reported in this paper.

References

1. Bertolini, L.; Elsener, B.; Pedeferri, P.; Polder, R.B. *Corrosion of Steel in Concrete: Prevention, Diagnosis, Repair*; Wiley-VCH: Weinheim, Germany, 2004.
2. Broomfield, J.P. *Corrosion of Steel in Concrete: Understanding, Investigation and Repair*, 2nd ed.; Taylor & Francis: London, UK, 2007.
3. Archie, G.E. The electrical resistivity log as an aid in determining some reservoir characteristics. *Trans. AIME* **1942**, *146*, 54–62. [CrossRef]
4. McCarter, W.J.; Broadbent, A.M. Electrical response of Portland cement pastes with special reference to admixtures. *Adv. Cem. Res.* **1994**, *6*, 1–9.
5. Villain, G.; Ihamouten, A.; Dérobert, X.; Sbartaï, Z.M. Use of electromagnetic NDT for the assessment of water and chloride contents in concrete: Calibration and adaptation in the laboratory before application in the field. *Constr. Build. Mater.* **2012**, *37*, 893–903. [CrossRef]
6. Lespinasse, M.; Villain, G.; Sbartaï, Z.M.; Dérobert, X. Application of ERT and GPR to the assessment of harbour structures. *Constr. Build. Mater.* **2018**, *181*, 624–633.
7. *BS EN 206:2013+A2:2021*; Concrete—Specification, Performance, Production and Conformity. British Standards Institution: London, UK, 2021.
8. *ASTM STP 1065*; The Threshold Concentration of Chloride in Concrete for the Initiation of Reinforcement Corrosion. ASTM International: Philadelphia, PA, USA, 1990.
9. Loke, M.H.; Barker, R.D. Rapid least-squares inversion of apparent resistivity pseudosections by a quasi-Newton method. *Geophys. Prospect.* **1996**, *44*, 131–152. [CrossRef]
10. Daniels, D.J. *Ground Penetrating Radar*, 2nd ed.; Institution of Engineering and Technology: London, UK, 2004.
11. Karhunen, K.; Seppänen, A.; Lehikoinen, A.; Monteiro, P.J.M.; Kaipio, J.P. Electrical resistance tomography imaging of concrete. *Cem. Concr. Res.* **2010**, *40*, 137–145. [CrossRef]
12. Polder, R.B. Test methods for on-site measurement of resistivity of concrete—A RILEM TC-154 technical recommendation. *Constr. Build. Mater.* **2001**, *15*, 125–131. [CrossRef]
13. Poupard, O.; L'Hostis, V.; Catinaud, S.; Petre-Lazar, I. Corrosion damage diagnosis of a reinforced concrete beam after 40 years natural exposure in marine environment. *Cem. Concr. Res.* **2006**, *36*, 504–520. [CrossRef]
14. Elsener, B. Half-cell potential measurements—Potential mapping on reinforced concrete structures. *Mater. Struct.* **2002**, *36*, 461–471.
15. Andrade, C.; Alonso, C. Test methods for on-site corrosion rate measurement of steel reinforcement in concrete by means of the polarization resistance method. *Mater. Struct.* **2004**, *37*, 623–643. [CrossRef]
16. Hugenschmidt, J. Concrete bridge inspection with a mobile GPR system. *Constr. Build. Mater.* **2002**, *16*, 147–154. [CrossRef]
17. Shaw, M.R.; Millard, S.G.; Molyneaux, T.C.K.; Taylor, M.J.; Bungey, J.H. Location of steel reinforcement in concrete using ground penetrating radar and neural networks. *NDT E Int.* **2005**, *38*, 203–212. [CrossRef]
18. Sbartaï, Z.M.; Laurens, S.; Balayssac, J.P.; Ballivy, G.; Arliguie, G. Effect of concrete moisture on radar signal amplitude. *ACI Mater. J.* **2006**, *103*, 419–426. [CrossRef]

Disclaimer/Publisher's Note: The statements, opinions and data contained in all publications are solely those of the individual author(s) and contributor(s) and not of MDPI and/or the editor(s). MDPI and/or the editor(s) disclaim responsibility for any injury to people or property resulting from any ideas, methods, instructions or products referred to in the content.